



Photocatalytic oxidation of gas-phase Hg^0 by CuO/TiO_2

Jiang Wu^{a,*}, Chaoen Li^a, Xuying Zhao^a, Qiang Wu^a, Xuemei Qi^a,
Xiantuo Chen^a, Tao Hu^a, Yan Cao^{b,**}

^a College of Energy and Mechanical Engineering, Shanghai University of Electric Power, Shanghai 200090, China

^b Institute for Combustion Science and Environmental Technology, Western Kentucky University, KY 42101, USA

ARTICLE INFO

Article history:

Received 28 January 2015

Received in revised form 5 April 2015

Accepted 12 April 2015

Available online 21 April 2015

Keywords:

Mercury

TiO_2

CuO

Photocatalysis

Gas-phase Hg^0

ABSTRACT

A simplified approach for the fabrication of CuO/TiO_2 was demonstrated. In this study, low cost CuO/TiO_2 photocatalysts (CuO loading 0–15 wt.%) were prepared, characterized and evaluated for gas-phase Hg^0 oxidation. The obtained CuO/TiO_2 photocatalysts were used to remove gaseous elemental mercury under UV light and visible light (both xenon lamp and LED), respectively, and the optimum doping levels of CuO and optimum illumination conditions were determined. The results showed that the CuO/TiO_2 photocatalysts were highly efficient in oxidizing Hg^0 , reaching above 70% in all cases under UV light, peaking at 57.8% with 1.25 wt.% CuO under visible light and peaking at about 60% with 1.25 wt.% CuO under LED light. We have proposed that the probable mechanism by which CuO/TiO_2 photocatalysts removes gaseous elemental mercury is two-fold: the CuO not only prevents electrons and holes from recombining, but also narrows the band gap of TiO_2 .

© 2015 Published by Elsevier B.V.

1. Introduction

Because of its toxicity, high volatility, and persistent bioaccumulation in the environment, mercury emission has caused a serious threat to human health [1]. Mercury emitted from coal-fired power plant is a major anthropogenic source. Many countries have enforced mercury emission controls from coal-fired power plants. On December 21, 2011, the US Environment Protection Agency (EPA) announced the Mercury and Air Toxics Standards (MATS) to regulate mercury, acid gases and other toxic pollution from coal-fired power plants and the official bill took effect on April 16, 2012 [2]. The Ministry of Environmental Protection of China promulgated new emission standard of air pollutants for power plants, which specified a cap of 0.03 mg/m^3 for mercury and its compounds after January 1, 2015 [3]. Therefore, improving the removal efficiency of mercury from power plant is an urgent issue.

Mercury in the flue gas of coal combustion exists in three chemical forms: elemental mercury (Hg^0), particulate-bound mercury (Hg^{p}), and oxidized mercury (Hg^{2+}) [4–6]. Hg^{2+} is water-soluble, so it can be removed by wet scrubbers and the Hg^{2+} removal efficiency can reach up to 90% [5,7]. In addition, Hg^{p} can be easily removed by electrostatic precipitator (ESP) or fabric filter (FF)

[8]. However, Hg^0 is difficult to remove because of its volatility, insolubility and chemical stability [9]. So the most critical step is to control elemental mercury. There are two main methods for elemental mercury control: adsorption and oxidation. Activated carbon injection has proven to be an effective adsorption method for elemental mercury removal in flue gas [10]. However, its high operation cost and negative effect on fly ash quality may restrict its industrial application [11]. The drawbacks associated with the use of particulate adsorbents make the oxidation method more attractive. In recent years, the progress in the photocatalytic oxidation of Hg^0 has drawn renewed interests among researchers [12,13]. Compared with other methods, photocatalytic oxidation possesses higher oxidation ability and no secondary pollution, therefore, it is a promising technology for oxidation of elemental mercury.

TiO_2 is one of the most widely recognized semiconductor photocatalysts for oxidation of elemental mercury, because of its nontoxicity, low cost, and high chemical stability. However, TiO_2 can only be excited by ultraviolet (UV) irradiation, which accounts for merely about 4% of the total solar radiation. In addition, low rate of electron transfer and high rate of recombination between excited electron-hole pairs often result in low quantum yield rate and a limited photooxidation rate [14,15]. Many researchers tried a lot of methods to modify the photocatalyst to make photocatalysis under visible light more practical and improve photocatalytic oxidation efficiency. These methods include surface modification [16,17], metal or nonmetal ion doping [18–20], combining with other semiconductors or metal oxides [21,22], etc. Among these methods, doping metal oxides into TiO_2 is an attractive method

* Corresponding author at: NO. 2103 Pingliang Road, Shanghai 200090, China. Tel.: +86 21 35303902/13761615154.

** Corresponding author at: 2413 Nashville Road, Bowling Green, KY 42101-4101, USA. Tel.: +1 270 745 2530.

E-mail addresses: wjcf2002@sina.com (J. Wu), yan.cao@wku.edu (Y. Cao).

to prevent the recombination of charge carriers and decrease the band gap. So the photocatalytic efficiency could be improved and the response range could expand to visible light region. CuO is one of the low-cost transition metal oxides. CuO has been regarded as a good active component for the reduction of water under sacrificial condition [23–26], because it can prevent the recombination between photogenerated electrons and holes. At the same time, it can decrease the energy of the band gap. However, there have been few studies reporting the use of CuO catalyst supported on TiO₂ as a system for Hg⁰ photocatalytic oxidation. Furthermore, few studies reported the effect of different light sources on the photocatalytic oxidation.

The aim of this study was to investigate the Hg⁰ oxidation efficiencies of CuO catalyst doped TiO₂. The effect of different light sources on Hg⁰ photocatalytic oxidation was studied. Furthermore, TGA (thermo-gravimetric analysis), XRD (X-ray diffraction), SEM-EDAX (scanning electron microscope and energy-dispersive X-ray spectroscopy), TEM (transmission electron microscope), UV-vis (Ultraviolet-visible spectroscopy), BET (the Brunauer, Emmett, and Teller) and PL (photoluminescence) were applied to characterize the catalysts, and the reaction mechanism was discussed based on the experimental and characterization results. This study provides information regarding the industrial applications of CuO/TiO₂ photocatalyst.

2. Experimental

2.1. Chemicals and materials

Copper nitrate hemihydrate (98%), glycerol (≥99%), sodium hydroxide (≥98%) were all obtained from Guoyao Chemical Reagent Co., Ltd., and used without further purification. Degussa P25 TiO₂ (85 wt.% Anatase, 15 wt.% Rutile, ≥99.5%) was obtained from a local supplier. All solution was prepared using ultrapure water.

2.2. Preparation of CuO/TiO₂ photocatalyst

CuO/TiO₂ photocatalysts with nominal CuO loading of 0–15 wt.% were prepared by the complex precipitation method described by Yoong et al. [27]. Briefly, copper nitrate hemihydrate and glycerol (mole ratio of 1:2) were added to ultrapure water (100 mL) to form an aqueous copper(II)-glycerol complex. The masses of copper nitrate hemihydrate and glycerol used depended on the nominal CuO loading. P25 TiO₂ (5.0 g) was added to the solution continuous stirring. The copper-glycerol complex was then precipitated on the TiO₂ support by the drop wise addition of 0.5 M NaOH under constant stirring until pH to 12. The resulting suspension was stirred for a further 1 h, then the light blue powders (presumably Cu(OH)₂/TiO₂) were collected by centrifugal separation. After washing repeatedly with ultrapure water, the Cu(OH)₂/TiO₂ powders were obtained by drying overnight at 70 °C in air. CuO/TiO₂ photocatalysts were obtained by calcination of the Cu(OH)₂/TiO₂ powders at 300 °C for 2 h.

2.3. CuO/TiO₂ photocatalyst characterization

TGA analyses were performed on a NETZSCH STA 409 PC/PG thermogravimetric analyzer. Photocatalyst precursor, Cu(OH)₂/TiO₂, was heated in air from room temperature to 800 °C at heating rate of 10 °C/min.

UV-vis absorbance spector were recorded over the range 250–800 nm on a UV-vis spectrophotometer (SHIMADZU UV-3600, Japan). Barium sulfate (BaSO₄) was used as a reference standard.

The morphology of the catalyst was determined using a scanning electron microscope (SEM, Phillips XL-30 FEG/NEW), equipped with an EDAX corporation energy dispersive X-ray analysis (EDAX)

system for quantitative analysis of elements present in each sample. Specimens were mounted on double-sided carbon tape and lightly platinum sputter coated for analysis.

TEM images were collected on a Phillips Model CM200 transmission electron microscope. Powders samples were dispersed in absolute ethanol and then dispersed on holey carbon coated copper TEM grids for analysis.

Powder XRD patterns were taken on a BRUKER D8 ADVANCE Diffractometer. XRD data was collected from 2θ = 10–90° (step 0.02°, scan rate 2° min^{−1}) using Cu Kα X-rays (λ = 1.5418 Å, 40 mA, 40 kV). Anatase and Rutile crystallite sizes were determined from the powder XRD data using the Scherrer equation and line-widths of Anatase (1 0 1) reflection at 2θ = 25.3° and Rutile (1 1 0) reflection at 2θ = 27.4°, respectively. The Rutile:Anatase ratio in the samples was determined according to the method described by Ding et al. [28]

$$\% \text{Rutile} = \frac{1}{[1 + 0.8(I_A + I_R)]} \times 100 \quad (1)$$

where I_A is the peak intensity for Anatase (1 0 1) reflection, and I_R is peak intensity for the Rutile (1 1 0) reflection.

N₂ physisorption isotherms were determined at liquid nitrogen temperature (−195 °C) using a Micromeritics ASAP 2020 instrument. Specific surface areas were calculated from the N₂ adsorption data according to the Brunauer–Emmett–Teller (BET) method using P/P_0 values in the range 0.05–0.2 [29]. Cumulative pore volumes and pore diameters were calculated from the adsorption isotherms by the Barrett–Joyner–Halenda (BJH) method [30]. Samples were degassed at 80 °C under vacuum for 6 h prior to the N₂ physisorption measurements.

Photoluminescence measurements were performed in air at room temperature using a fluorescence spectrophotometer (SHIMADZU RF5301, Japan). A 290 nm cut off filter was used. Spectra were excited at 310 nm and photoluminescence spectra were recorded over a range of 330–600 nm using a standard photomultiplier.

2.4. Measurement of photoactivity

The schematic diagram of the experimental system is shown in Fig. 1. The system consisted of simulated flue gas, a photocatalytic reactor and a mercury analyzer. The N₂ was divided into two branches, whose flow rates were controlled by two mass flow meters (MFC, CS200 type) separately. The total flow of the two branches was 1.2 L/min. One gas stream with a flow rate of 0.2 L/min passed through the Hg⁰ permeation tube to introduce Hg⁰ vapor into the system. The Hg⁰ inlet concentration was around 65 μg/m³. The mercury permeation tube was placed in a U-shape glass tube which was immersed in a constant 55 °C water bath to ensure a constant Hg⁰ permeation rate. The other stream of N₂ had a flow rate of 1 L/min. An on-line mercury analyzer (VM3000 mercury vapor monitor, Mercury Instruments, Germany) based on atomic absorption spectrometry was used to measure the gas phase concentration of Hg⁰. The gas flowed through two silica gel columns before entering the mercury analyzer to remove water vapor. Finally, the gas got through the active carbon bottle and vented out of the system.

The catalyst (50 mg) was coated on quartz glass plates (75 mm × 75 mm) by using a dip-coating method, then it was put into the photocatalytic reactor developed by ourselves, which is shown in Fig. 2. The photocatalytic reactor was consisted of inlet transition zone, reaction zone and outlet transition zone.

The reaction zone had quartz glass cover plate on top, so light could reach the surface of the catalyst through the cover board. Reflective device was placed around the tubes, making the illumination uniform throughout the reaction zone. The simulated flue gas containing mercury went through the inlet transition zone

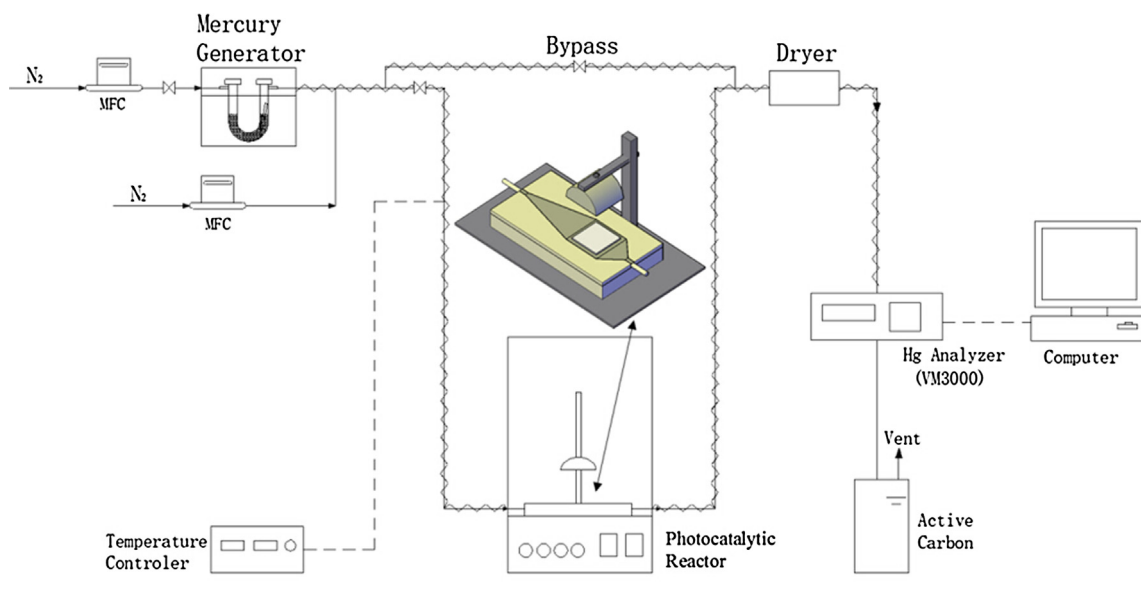


Fig. 1. Schematic diagram of the experimental system.

between the inlet and the reaction zone and accepted the light to complete the photocatalytic oxidization process. The inlet transition zone made the flow field in the reaction zone uniform so that the reaction process would not be distorted by nonuniform flow field and better simulate the flow field in the flue gas duct in coal-fired power plants.

In this work, in order to describe this phenomenon in detail, the Hg^0 removal efficiency under light irradiation condition was defined as following:

$$n = \frac{\text{Hg}_{\text{in}}^0 - \text{Hg}_{\text{out}}^0}{\text{Hg}_{\text{in}}^0} \times 100\% \quad (2)$$

where Hg_{in}^0 represented Hg^0 ($\mu\text{g}/\text{m}^3$) at the inlet of the reactor, and Hg_{out}^0 represented Hg^0 ($\mu\text{g}/\text{m}^3$) at the outlet of the reactor.

3. Results and discussions

3.1. CuO/TiO_2 photocatalyst characterization

3.1.1. TGA analysis

Fig. 3(a) shows TGA curves for the 1.25 wt.%, 10 wt.% and 15 wt.% CuO/TiO_2 photocatalyst precursors with heating in air from room

temperature to 800°C . The precursor was $\text{Cu}(\text{OH})_2$ supported on TiO_2 . All sample showed a 1–5% mass loss below 200°C due to thermal desorption of surface chemisorbed water. Between 200 and 350°C , thermal decomposition of supported $\text{Cu}(\text{OH})_2$ to CuO and H_2O occurred [27,31]. Mass losses in this range increased in proportion to $\text{Cu}(\text{OH})_2$ content in the sample. The mass loss at $\sim 600^\circ\text{C}$ was due to thermal reduction of CuO to Cu_2O [32]. The TGA data indicated that precursor calcination at 300°C for 2 h was appropriate for preparing CuO/TiO_2 photocatalysts, ensuring complete thermal pyrolysis of supported $\text{Cu}(\text{OH})_2$ to CuO . Fig. 3(b) demonstrates the process of CuO generation, the result agreed with TEM analysis which is shown in Fig. 6.

3.1.2. The appearance of photocatalysts and SEM observation

Fig. 4 shows a photograph of the 0–15 wt.% CuO/TiO_2 photocatalysts calcinated at 300°C for 2 h. At low CuO loading (0.31–1.25 wt.%), the CuO/TiO_2 samples were all light blue–green in color as was typical for octahedrally coordinated $\text{Cu}(\text{II})$ cations [33]. At CuO loading of 2.5 wt.% or more, the CuO/TiO_2 photocatalysts were all grey, and the intensity of grey color increased proportionately with higher CuO loading levels. Because CuO was black and

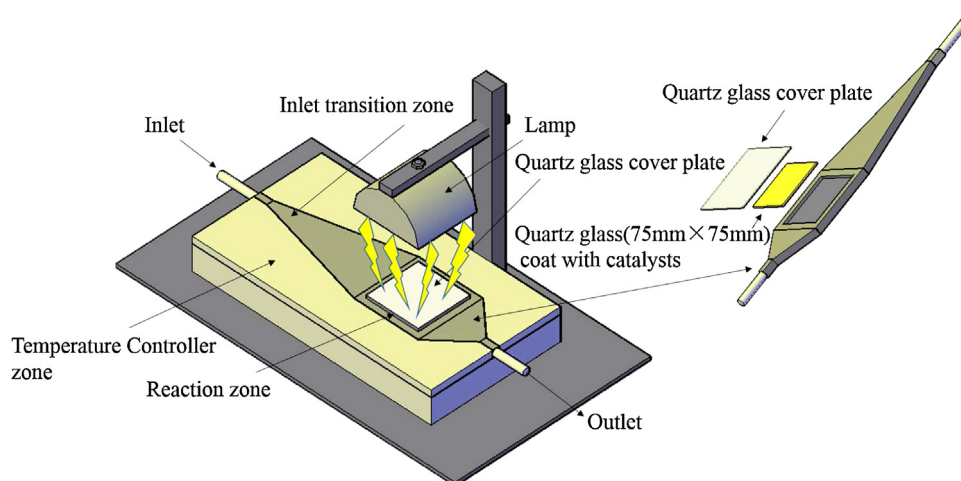


Fig. 2. Schematic of the photocatalytic reactor.

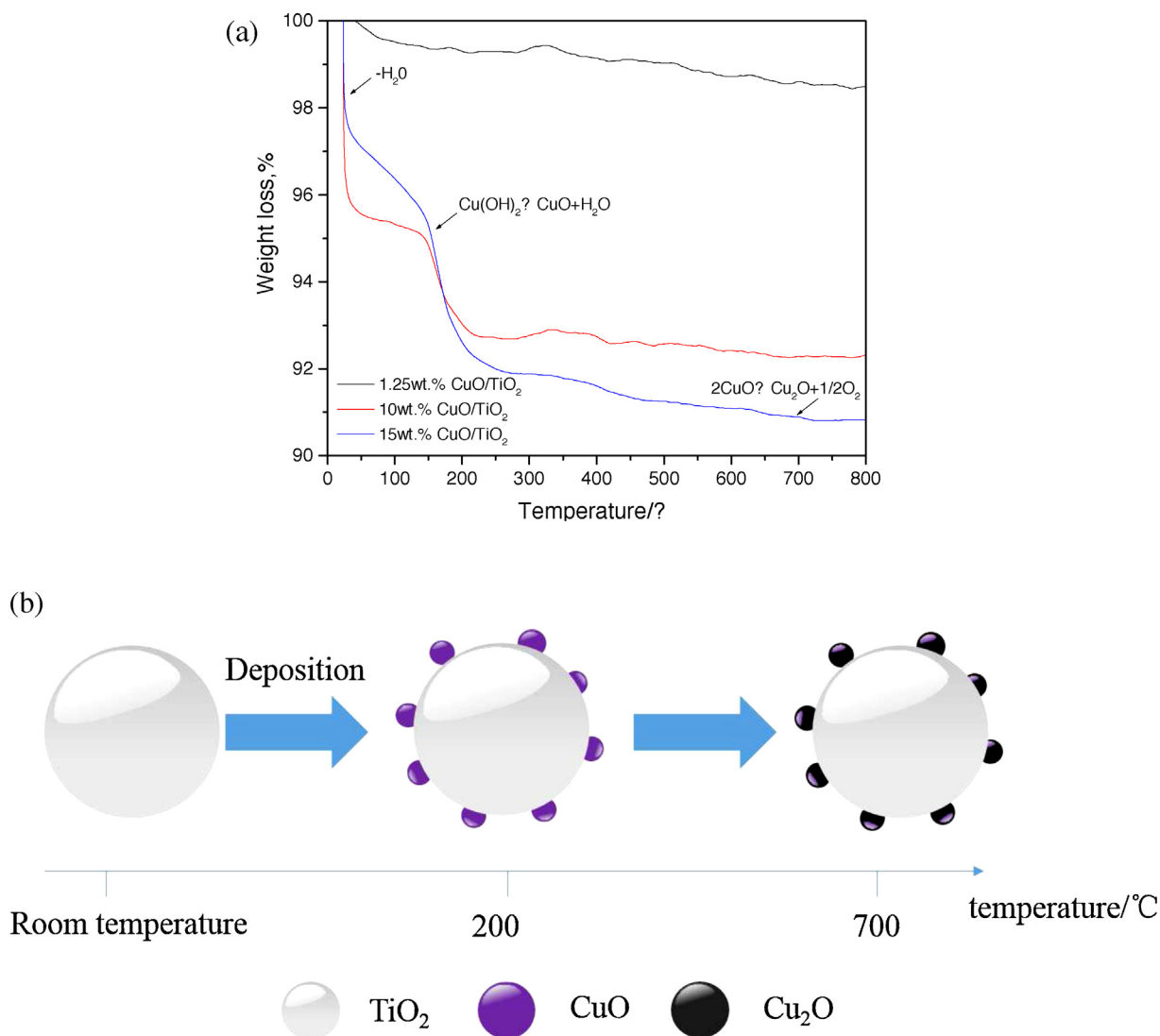


Fig. 3. (a) TGA curves for selected CuO/TiO₂ photocatalyst precursors in air (heating rate 10 °C min⁻¹). Important thermal transitions are shown on the figure. (b) Scheme of generation process by CuO.

TiO₂ is white, so the grey color of the 2.5–15 wt.% CuO/TiO₂ samples suggested the formation of CuO nanoparticles on the surface of the TiO₂. XRD data shown in Fig. 7 confirms the appearance of a discrete CuO phase for the 2.5–15 wt.% CuO/TiO₂ powders. Difference in the appearance of the CuO/TiO₂ photocatalysts prepared at low loading (<2.5 wt.% CuO) and high loading (2.5 wt.% CuO or above)

strongly suggested that the electronic state of CuO(II) was different among these sets of samples. This viewpoint will be elaborated in detail below.

To attain CuO content in the CuO/TiO₂ photocatalysts and the nanoporous structures, the FSEM/EDAX micrographs of CuO/TiO₂ are shown in Fig. 5. The morphology of the catalyst with different



Fig. 4. Photograph of the 0–15 wt.% CuO/TiO₂ photocatalysts. (For interpretation of the references to color in the text, the reader is referred to the web version of this article.)

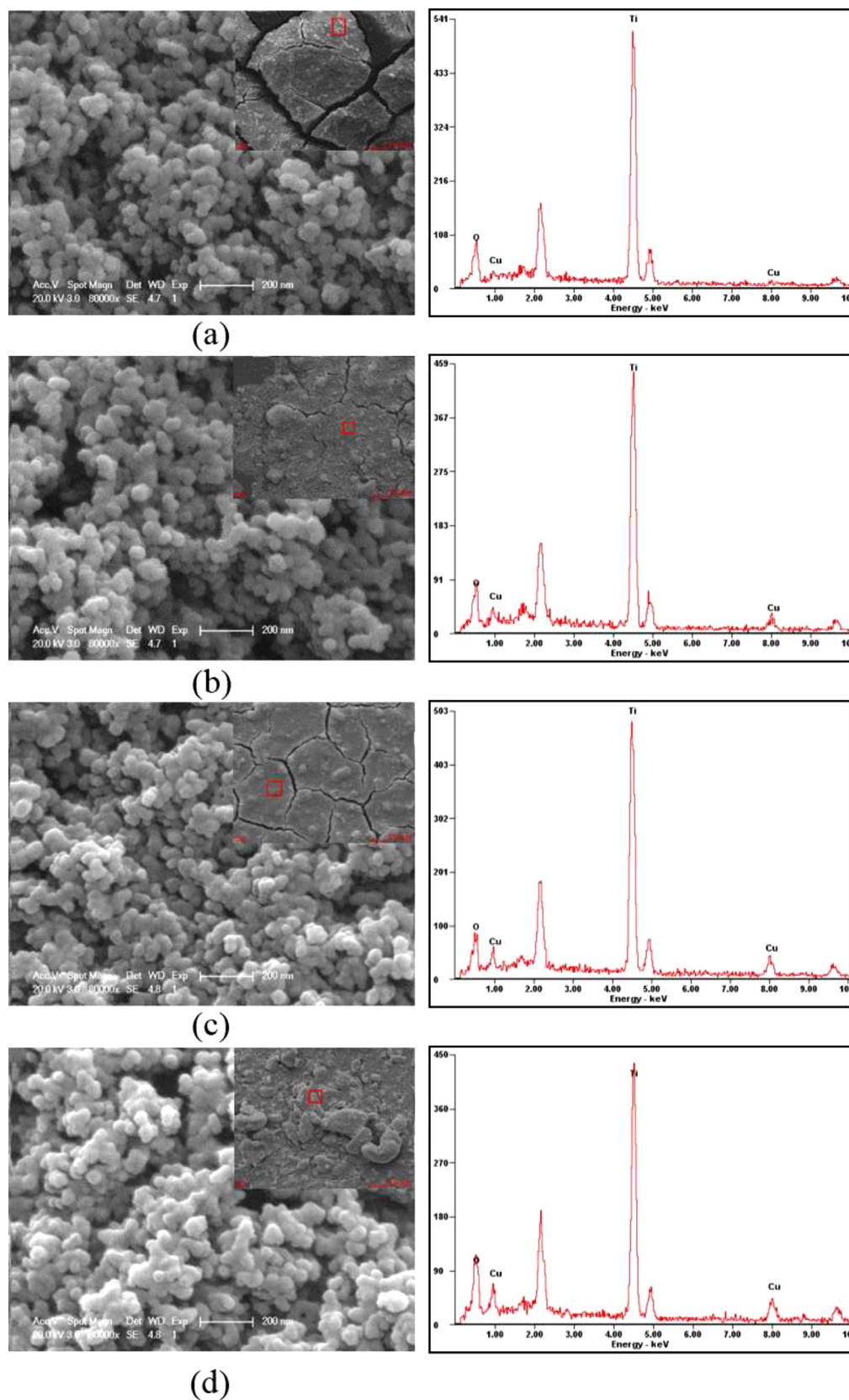


Fig. 5. FESEM images (left) and EDAX spectra (right) for selected CuO/TiO₂ photocatalysts: (a) 1.25 wt.% CuO/TiO₂; (b) 5 wt.% CuO/TiO₂; (c) 10 wt.% CuO/TiO₂; (d) 15 wt.% CuO/TiO₂. Pt in the EDAX spectra originated from the Pt sputter coating of samples for FESEM analysis.

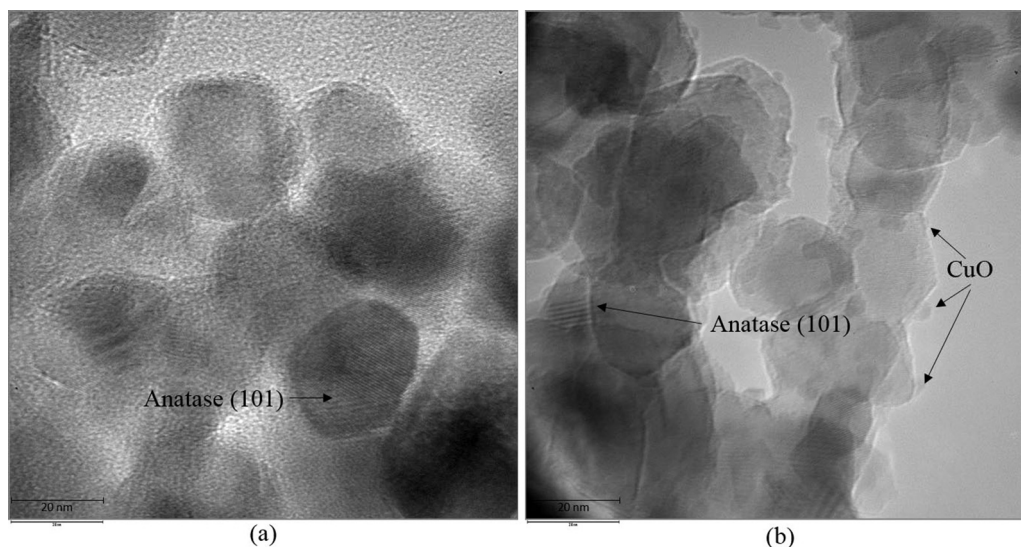


Fig. 6. TEM images of (a) 1.25 wt.% CuO/TiO₂; (b) 10 wt.% CuO/TiO₂.

Table 1

Summary of the physical, chemical and photocatalytic properties of the 0–15 wt.% CuO/TiO₂ photocatalysts.

CuO loading (wt.%)	Absorbing boundary (nm)	Bandgap (eV)	CuO content by EDAX (wt.%)	BET surface area (m ² /g)	Pore volume (cm ³ /g)	Pore diameter (nm)	Hg ⁰ removal efficiency (visible light) η (%)
TiO ₂	394	3.15	–	47.65	0.176	16.02	19.9
0.31	464	2.67	–	43.83	0.460	43.07	54
0.63	512	2.42	–	46.04	0.457	39.92	47
1.25	540	2.29	1.1	47.26	0.315	31.01	57.9
2.5	600	2.07	–	46.98	0.388	36.41	42.7
5	612	2.03	5.5	46.84	0.308	31.46	45.3
7.5	628	1.97	–	46.49	0.357	37.30	37
10	645	1.98	9	42.18	0.386	43.83	20.2
15	718	1.73	14.7	42.41	0.351	40.68	7.3
CuO	–	1.34	–	31.37	0.268	27.36	3

CuO doping ratio showed no significant difference compared with the P25. When the concentration of doped CuO went above 5 wt.%, the catalyst began to have slight aggregation. As shown in Fig. 5, Cu, Ti and O appeared in all of the samples. Even when CuO doping amount was low, Cu²⁺ was still detected on the surface of TiO₂. And with the increase of CuO doping, CuO content in the sample also showed gradual increase. From the EDAX analyses (Table 1), CuO content in the CuO/TiO₂ photocatalysts was almost identical to the actual CuO loading.

3.1.3. TEM analysis

TEM was used to examine the dispersion of CuO over the TiO₂ support as a function of CuO loading. TEM images for selected CuO/TiO₂ photocatalysts are shown in Fig. 6. The TEM image for the 1.25 wt.% CuO/TiO₂ photocatalyst (Fig. 6(a)) was characteristic for the P25 TiO₂ support, composed of small spherical Anatase TiO₂ crystallites of ~20–30 nm diameter and larger angular crystallites of Rutile TiO₂ (diameter 40–60 nm). There were no individual CuO particles seen, though copper was detected by EDAX analysis. This indicated that at low CuO loadings, Cu²⁺ was highly dispersed over the TiO₂ support. At higher loadings, particularly 10 wt.% CuO, discrete CuO nanoparticles could be seen on the TiO₂ support particles (Fig. 6(b)). The average diameter of the CuO nanoparticles was approximately 2–4 nm. The CuO nanoparticles appeared to develop preferentially on the Anatase TiO₂ support particles. The TEM data of Fig. 6 suggested that CuO nanoparticle formation occurs only after the CuO loading exceeded a few percentage points by weight.

3.1.4. XRD analysis

The XRD pattern of the CuO/TiO₂ series of catalysts are depicted in Fig. 7. The XRD patterns for all samples were dominated by peaks due to Anatase and Rutile in the TiO₂. From the relative intensity of the Anatase (1 0 1) and Rutile (1 1 0) reflection, the Anatase:Rutile weight ratio in the P25 TiO₂ support was estimated to be 6:1, in good agreement with the manufacturer's specifications. Interestingly, Rutile (1 1 0) disappeared when the doping of CuO reached 5 wt.%, and then appeared again at higher doping of CuO (Fig. 7(g)).

Fig. 8 shows an expanded view of the XRD patterns in the 2 θ range 30–50°, where the most intense CuO reflection occurred. From the picture, there was no characteristic CuO peak in the catalysts when the CuO loading was less than 5 wt.%, indicating that the crystalline phase of CuO was too small to be detected in the TiO₂ phase. Well-dispersed active elements in the catalyst can enhance the catalytic activity [34]. However, when the doped CuO was 7.5 wt.% or above, monoclinic CuO peaks intensified with CuO loading increasing. The XRD data confirmed that the dispersed state of CuO on TiO₂ had undergone a dramatic change in the CuO loading range of 5–7.5 wt.%.

3.1.5. UV–vis DRS and BET

The optical properties of 0–15 wt.% CuO/TiO₂ photocatalysts were studied with ambient temperature absorption spectroscopy from 250 nm to 800 nm, as shown in Fig. 9. All the as-prepared samples displayed intense absorption of light with wavelength below 400 nm. The visible light absorption spectra differed considerably depending on CuO loading, but the deposition of CuO caused all

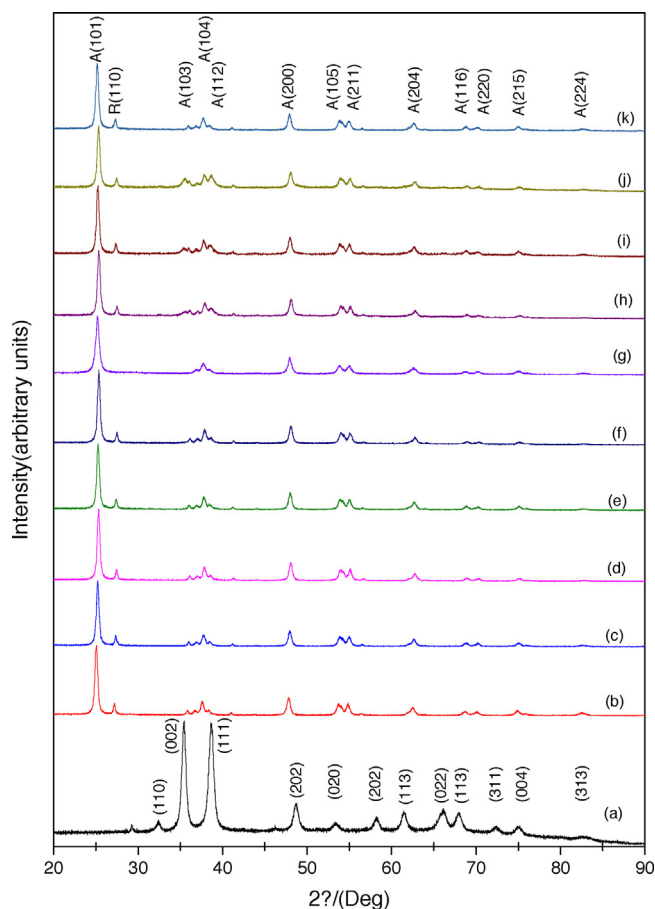


Fig. 7. Powder XRD patterns for the 0–15 wt.% CuO/TiO₂ photocatalysts after calcination at 300 °C for 2 h: (a) CuO; (b) P25 TiO₂; (c) 0.31 wt.% CuO/TiO₂; (d) 0.63 wt.% CuO/TiO₂; (e) 1.25 wt.% CuO/TiO₂; (f) 2.5 wt.% CuO/TiO₂; (g) 5 wt.% CuO/TiO₂; (h) 7.5 wt.% CuO/TiO₂; (i) 10 wt.% CuO/TiO₂; (j) 15 wt.% CuO/TiO₂; and (k) 1.25 wt.% CuO/TiO₂ (after reaction, under UV irradiation).

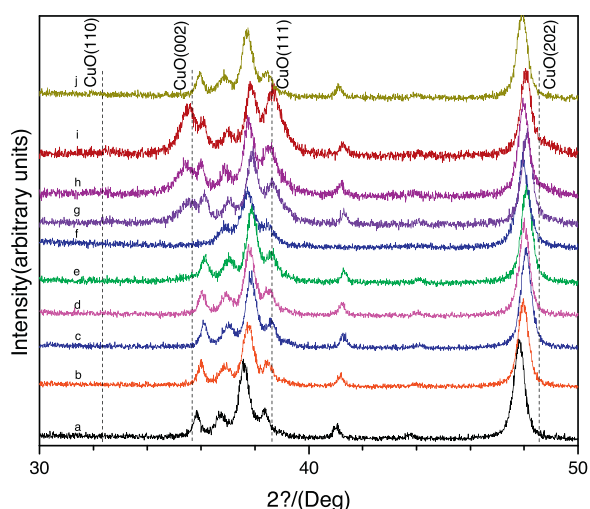


Fig. 8. Powder XRD patterns for the 0–15 wt.% CuO/TiO₂ photocatalysts after calcination at 300 °C for 2 h: (a) P25 TiO₂; (b) 0.31 wt.% CuO/TiO₂; (c) 0.63 wt.% CuO/TiO₂; (d) 1.25 wt.% CuO/TiO₂; (e) 2.5 wt.% CuO/TiO₂; (f) 5 wt.% CuO/TiO₂; (g) 7.5 wt.% CuO/TiO₂; (h) 10 wt.% CuO/TiO₂; (i) 15 wt.% CuO/TiO₂; and (j) 1.25 wt.% CuO/TiO₂ (after reaction, under UV irradiation).

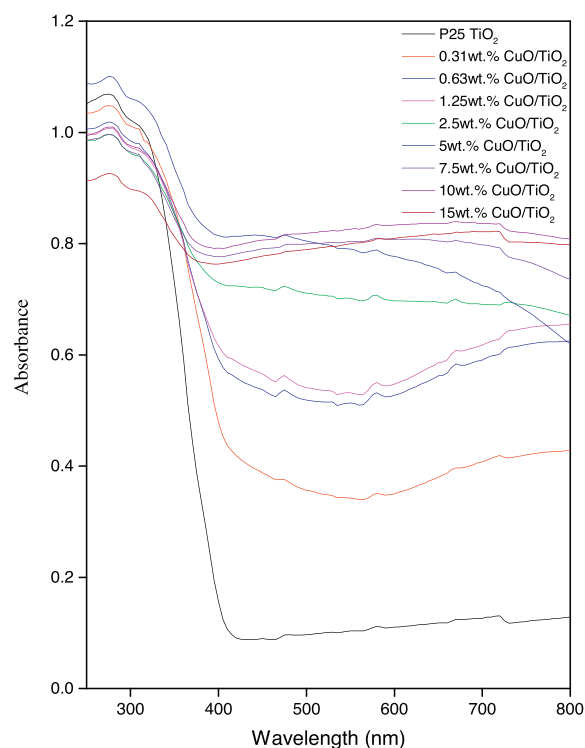


Fig. 9. UV–vis absorbance spectra of the 0–15 wt.% CuO/TiO₂ photocatalysts.

the samples to absorb visible light strongly. At low CuO loading (<2.5 wt.% CuO), absorption features at the wavelength of around 450 nm or above 800 nm were distinct, consistent with blue–green color of the samples (Fig. 4). At higher loadings (2.5 wt.% CuO or above), intense absorption across the entire visible spectrum was observed, consistent with CuO nanoparticle formation (bulk CuO absorbs very strongly between 300 and 800 nm). From the UV–vis data of Fig. 9, it could be qualitatively seen that the electric state of CuO(II) differed between the low and high CuO loading samples. Lastly, the optical band gap energy (E_g) of the 0–15 wt.% CuO/TiO₂ photocatalysts were calculated based on the absorption spectrum of the samples according to equation of $E_g = 1240/\lambda_{\text{Absorp.Edge}}$ [35]. The results are shown in Table 1. The data showed that the absorption edge of the CuO/TiO₂ photocatalysts progressively shifted to lower energy with increasing levels of CuO loading.

Table 1 summarizes N₂ physisorption data for the CuO/TiO₂ photocatalysts. All samples, including the TiO₂, had similar N₂ physisorption isotherms that could be classified as Type II according to IUPAC convention for adsorption isotherms. When the CuO doping was above 1.25 wt.%, the BET surface areas of the photocatalysts generally decreased as the CuO loading increased.

3.1.6. Photoluminescence spectra

The photoluminescence (PL) emission spectra was widely used to investigate the efficiency of charge carrier transfer and the life time of photogenerated electron–hole in semiconductors. Various studies using PL spectra also demonstrated a significant improvement in the separation of photogenerated carriers (as shown in Fig. 10) [23,25,27,36]. The intense nature of the photoluminescence signal observed for the P25 TiO₂ indicated that rapid electron–hole pair recombination occurred following light excitation. After doping TiO₂ with CuO, the PL intensity of all photocatalysts was weaker than P25 TiO₂, which indicated CuO effectively suppressed electron–hole pair recombination in TiO₂, even at moderate CuO loading. It was attributed to CuO doping as loaded CuO prevented

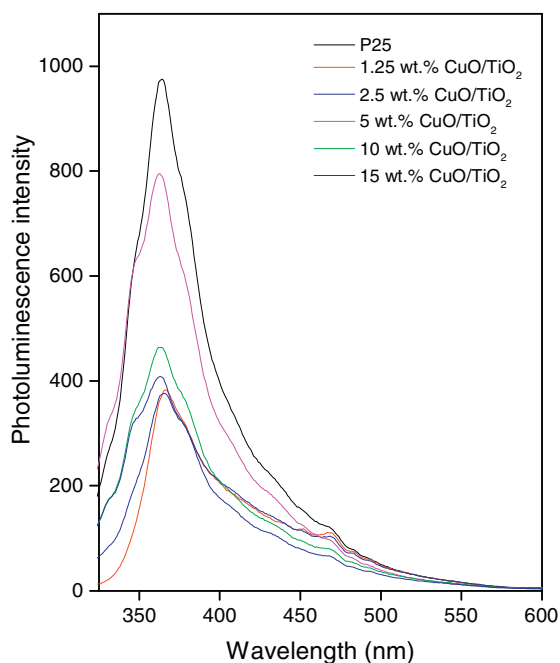


Fig. 10. Photoluminescence spectra for 0–15 wt.% CuO/P25 TiO₂ photocatalysts.

electrons and holes from recombining, which enhanced the photocatalytic activity of TiO₂ for Hg⁰ oxidation.

3.2. Photocatalytic properties

3.2.1. Effect of CuO content

The photocatalytic oxidation removal efficiency for Hg⁰ was studied. Each experiment was carried out for around 180 min. First, the photocatalytic oxidation efficiency of CuO/TiO₂ with different CuO doping ratio under ultraviolet light and simulated sunlight, xenon lamp conditions, was investigated. The results are shown in Fig. 11. The CuO by itself was unable to photocatalytically oxidize Hg⁰ under the irradiation of ultraviolet light or xenon lamp conditions because the edge energy of CuO ($E_g = 1.34$ eV) excited by UV light was not enough to produce $\bullet\text{OH}$. With the increase of CuO doping amount, mercury removal efficiency decreased but still above 70%, which was much higher than that of P25 TiO₂ under the irradiation of ultraviolet light. This was mainly due to the few Cu

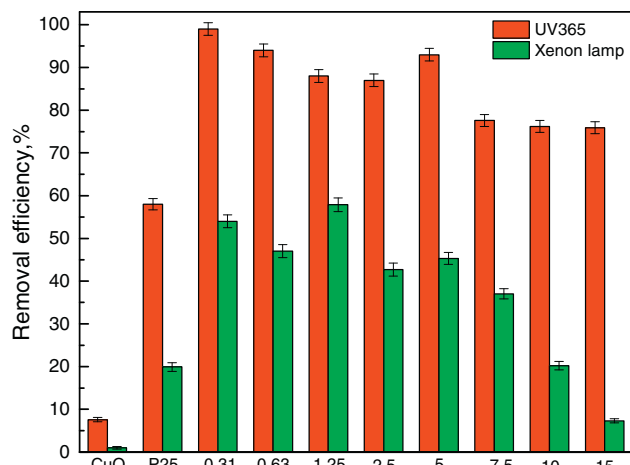
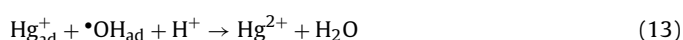
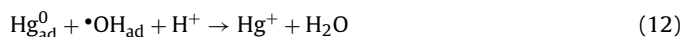


Fig. 11. Impact of CuO-doping concentration on the mercury removal efficiency of CuO/TiO₂ under UV365 light and visible light (xenon lamp).

ions doped into the TiO₂ lattice, which improved the photocatalytic efficiency. CuO effectively suppressed electron–hole pair recombination in TiO₂ even at moderate CuO loading [37]. But too much CuO loading resulted in a decrease in photocatalytic efficiency. The main reason was that too much CuO coverage on the surface of TiO₂ blocked the active sites [38]. Interestingly, when the CuO doping content was 5 wt.%, the efficiency was the highest when in the doping of CuO was higher than 1.25 wt.%. The main reason was that when the CuO doping content was 5 wt.%, Rutile disappeared (Fig. 7 curve g). As widely known, the band of Rutile was higher than that of Anatase, so Anatase was more easily excited by photon. So to improve the photocatalytic efficiency by decreasing the amount of Rutile in the catalyst could be a promising direction for future investigations.

Fig. 11 shows the results of the catalytic oxidation efficiency of Hg⁰ under sunlight (xenon lamp) excitation. When the CuO doping amount reached 1.25 wt.%, the mercury removal efficiency reached 57.8%, which was much higher than that of P25 under sunlight (xenon lamp). Pure TiO₂ had no photocatalytic activity under sunlight. However, a small amount of Fe ion in commercial P25 TiO₂ enhanced its photocatalytic activity [39], so that the mercury removal efficiency of the commercial P25 TiO₂ under sunlight could reach up to around 20%. At low CuO loading (1.25 wt.%), copper was existed as a sub-monolayer Cu(II) or CuO species on TiO₂ [37]. The Fermi level for such adsorbed species was positive with respect to the conduction band of TiO₂, resulting in transfer of photo-excited electrons from TiO₂ to the surface Cu(II) or CuO centers. At CuO loading above 1.25 wt.%, the rate of Hg⁰ oxidation decreased sharply. Pure CuO was inactive for Hg⁰ photocatalytic oxidation in this study (Fig. 11). Thus, the decreased activity of the CuO/TiO₂ photocatalysts at CuO loading above the optimal value of 1.25% was attributed to partial blockage of TiO₂ sites by supported CuO nanoparticle. This result indicated that the best Hg⁰ oxidation efficiency was observed for the 0.31–1.25 wt.% CuO/TiO₂ samples.

Under the light excitation, TiO₂ was active for Hg⁰ photocatalytic oxidation. The main reason was that TiO₂ produced photo-excited electrons and photo-excited holes, which could convert the water vapor adsorbed on the catalyst surface into H⁺ and OH[−] [40]. Then photo-excited holes turned OH[−] into $\bullet\text{OH}$, which was a strong oxidant. O₂ adsorbed on the catalyst surface was reduced by the photo-excited electrons, forming superoxide radicals $\bullet\text{O}_2^-$. Hg⁰ can be oxidized to Hg²⁺ by both $\bullet\text{O}_2^-$ and $\bullet\text{OH}$ [41]. The photocatalytic oxidation steps can be described as Eqs. (3)–(13) [40–43].



3.2.2. Effect of wavelength

Second, the photocatalytic oxidation efficiency of CuO/TiO₂ with the optimum 1.25 wt.% doping of CuO was investigated under dif-

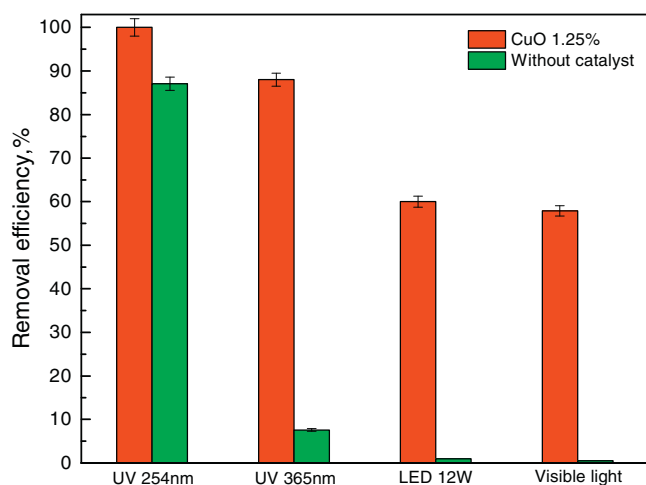
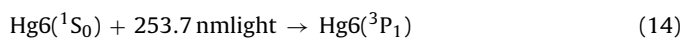


Fig. 12. Impact of light sources on the mercury removal efficiency of CuO/TiO₂.

ferent light irradiation, and the results are shown in Fig. 12. As seen in the graph, when using UV ($\lambda = 254$ nm) as the light source, even without catalyst the Hg⁰ removal efficiency reached up to above 85%, which was consistent with other studies [44]. Under this circumstance, the chemical reaction happened in the empty reactor was photochemical catalysis. The overall reaction between mercury and oxygen under the influence of 253.7 nm light was given by the overall global Reactions (14) and (15) [44]. Under UV irradiation, Hg6 (¹S₀) was transformed into Hg6 (³P₁), then collided with other gas atoms or molecules to complete the transition process from Hg6 (³P₁) to Hg6 (¹S₀). At the same time, Hg line at $\lambda = 253.7$ nm was the strongest resonance line of Hg, (³P₁–¹S₀), appearing in both absorption and emission. The analysis indicated that, although the nitrogen used was of ultrahigh purity (99.999%), it still contained some oxygen, water vapor, and hydrocarbons. Because the Hg concentration in the simulated flue gas was so little, the impurities in the nitrogen was sufficient to oxidize Hg under the UV light ($\lambda = 254$ nm). When using the catalyst, both photochemical reaction and photocatalytic reaction happened, and the mercury removal efficiency reached up to 100%.



When the wavelength of UV increased to 365 nm, the empty reactor was without the ability to remove mercury. The reason was that the light could not provide enough energy to directly turn Hg6 (¹S₀) into Hg6 (³P₁). The photocatalytic reaction became the dominant process. The reaction was described in Eqs. (3)–(13).

When the wavelength was expanded to the visible light range, the light had no effect on Hg atoms. So only photocatalytic reaction was occurring, producing free hydroxyl to oxidize Hg⁰. Interestingly, the photocatalytic efficiency generated by 12 W LED lamp was similar to that by the 400 W xenon lamp. The reason was that the LED light spectrum was monotonous, whose wavelength focused on 420 nm. Furthermore, LED lamp is highly efficient and energy conserving, so LED can be used as an optimal photocatalytic light source when no sunlight is available. Based on the above discussion, we propose that the photocatalytic reaction mechanisms under difference light sources are as described in Fig. 13.

Last but not least, the mercury removal efficiency under different LED intensity by changing the LED lamp power was studied. The results are shown as Fig. 14. In N₂ atmosphere, with the increase of LED wattage, the mercury removal efficiency increased slightly. According to Eq. (3), with the increase of light radiation intensity, the yield of •OH free radical increased, thereby it can enhance the

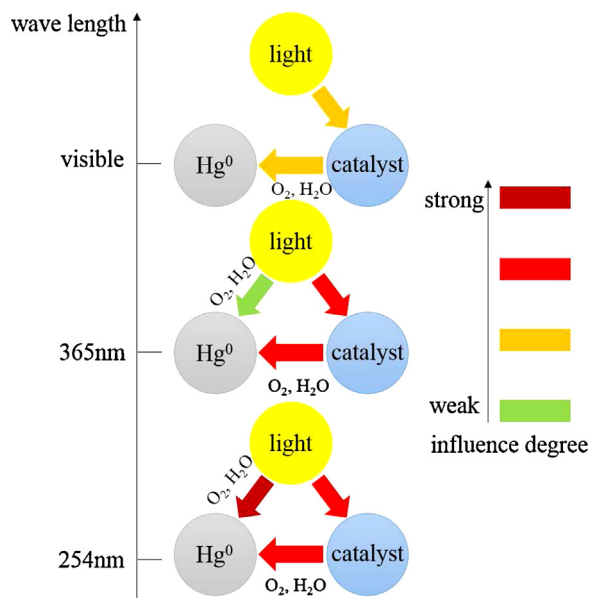


Fig. 13. Different relationship in the Hg⁰, light and catalyst under different light sources.

Hg⁰ removal ability, which agreed well with other studies [45]. When air was used as the carrier gas, the mercury removal efficiency was increased 10 percent points. As well known, when air was as the carrier gas, there was more oxygen in the reaction system, which can improve the oxidation efficiency, as shown in Eqs. (4)–(13).

3.2.3. Photocatalytic reaction mechanisms

Schematic diagram of charge carrier separation on the CuO/TiO₂ catalyst under the visible light are shown in Fig. 15. In this work, CuO/TiO₂ photocatalyst showed excellent mercury oxidation efficiency under visible light. The specific reasons were as follows: firstly, CuO doping prevented the recombination of photogenerated electrons and holes [37], which improved the efficiency of photocatalytic oxidation.

Secondly, electronic transition led the CuO/TiO₂ catalyst to be of high catalytic activity under visible light [36]. Indeed, the valence band level of TiO₂ or CuO/TiO₂, lied well below the redox reactions involving direction of Hg⁰ or the capture of free hydroxyl radicals.

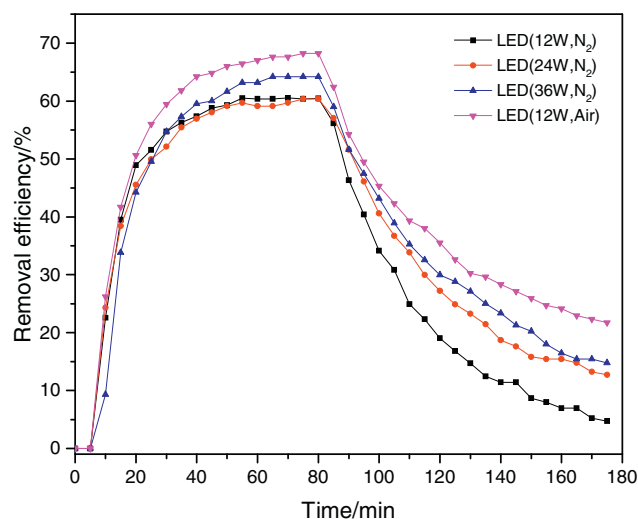


Fig. 14. Impact of light intensity and atmosphere on the mercury removal efficiency of CuO/TiO₂.

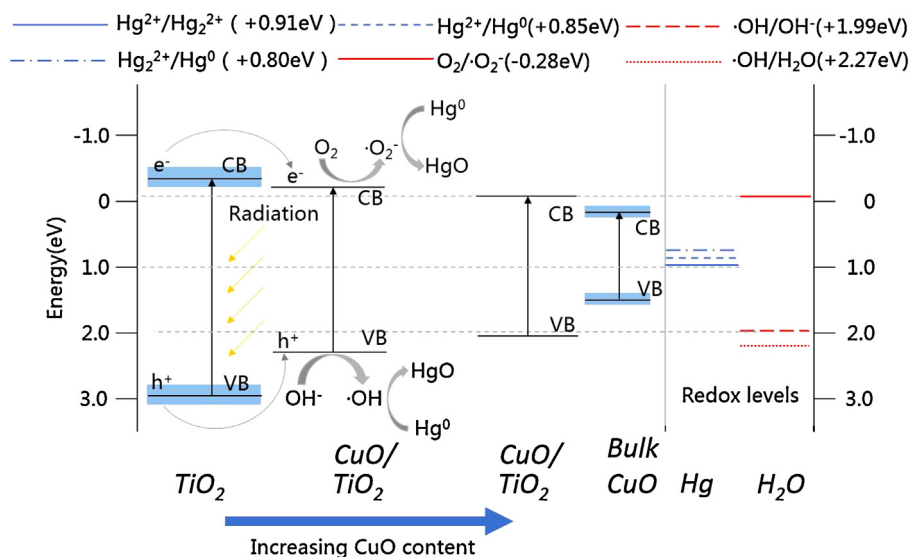


Fig. 15. Impact of light source on the mercury removal efficiency of CuO/TiO₂.

At low CuO loading, copper was existed as a sub-monolayer Cu(II) or CuO species on TiO₂ [37]. The Fermi level for such adsorbed species was positive with respect to the conduction band of TiO₂, resulting in transfer of photo-excited electron from TiO₂ to surface Cu(II) or CuO centers as shown in Fig. 15. That is why photocatalyst can oxidize Hg⁰ under visible light. Hg⁰ was oxidized by the photo-generated holes or free hydroxyl radicals [46–48]. With the loading ratio of CuO increasing, the conduction band of CuO/TiO₂ became positive with respect to O₂/·O₂[·] (−0.28 eV) couple, preventing transfer of electrons from CuO to O₂. At the same time, the valence band level of CuO/TiO₂ became negative with respect to ·OH/OH[·] (+1.99 eV) couple, weakening the ability of oxidation capacity. When the valence band level of catalyst was under that of ·OH/OH[·] (+1.99 eV), only the photo-generated holes oxidized the Hg⁰ and the efficiency was poor. In fact, under UV (4% of the total solar radiation) irradiation, little CuO was reduced to Cu₂O or Cu [49]. However, O₂ concentration is higher in flue gas than in water, and the existing O₂ can suppress CuO being reduced to Cu₂O or Cu. So, the negative effect on the Hg⁰ oxidation is not dramatic. Above all, the band gap of catalyst became narrow with the increase of CuO doping, but the ability of oxidation capacity also decreased. So, the oxidation efficiency of Hg⁰ decreased with too much CuO doping.

4. Conclusions

- 1) CuO/TiO₂ photocatalyst was prepared using the coprecipitation method with varying CuO doping levels. The photocatalyst obtained was in uniform particle form with grain size of 40–50 nm and BET surface around 45(m²/g).
- 2) The photocatalysts obtained had a high Hg⁰ removal efficiency under UV365 irradiation, above 70% in all cases. When the doping of CuO increased above 1.25%, the mercury removal efficiency under visible light irradiation decreased with higher doping of CuO.
- 3) Electronic transition was the mechanism behind the high efficiency of CuO/TiO₂ catalyst under visible light. LED can be used as photocatalytic light source when no sunlight is available.

Acknowledgment

This work was partially sponsored by (Natural Science Foundation (NSF), 21237003, 50806041).

References

- [1] N. Pirrone, S. Cinnirella, X. Feng, R. Finkelman, H. Friedli, J. Leaner, R. Mason, A. Mukherjee, G. Stracher, D. Streets, K. Telmer, Global mercury emissions to the atmosphere from natural and anthropogenic sources, in: R. Mason, N. Pirrone (Eds.), *Mercury Fate and Transport in the Global Atmosphere*, Springer, US, 2009, pp. 1–47.
- [2] U. EPA, Final Mercury and Air Toxics Standards (MATS) for Power Plants. Final Rule. <<http://www.epa.gov/airquality/powerplanttoxics/actions.html>>, (effective on 19.04.12).
- [3] Ministry of Environmental Protection (MEP) of China. Emission Standard of Air Pollutants for Thermal Power Plants, GB 13, 223–2011; MEP of China: Beijing, China, 2011.
- [4] R. Yan, D.T. Liang, L. Tsen, Y.P. Wong, Y.K. Lee, Bench-scale experimental evaluation of carbon performance on mercury vapour adsorption, *Fuel* 83 (2004) 2401–2409.
- [5] A.A. Presto, E.J. Granite, Survey of catalysts for oxidation of mercury in flue gas, *Environ. Sci. Technol.* 40 (2006) 5601–5609.
- [6] Z. Kwokal, N. Cukrov, V. Cuculi, Natural causes of changes in marine environment mercury speciation and distribution in anchialine caves, *Estuar. Coast. Shelf Sci.* 151 (2014) 10–20.
- [7] X. Xu, Q. Ye, T. Tang, D. Wang, Hg⁰ oxidative absorption by K₂S₂O₈ solution catalyzed by Ag⁺ and Cu²⁺, *J. Hazard. Mater.* 158 (2008) 410–416.
- [8] Y. Cao, B. Chen, J. Wu, H. Cui, J. Smith, C.-K. Chen, P. Chu, W.-P. Pan, Study of mercury oxidation by a selective catalytic reduction catalyst in a pilot-scale slipstream reactor at a utility boiler burning bituminous coal, *Energy Fuels* 21 (2006) 145–156.
- [9] S. Wu, M. Ozaki, M.A. Uddin, E. Sasaoka, Development of iron-based sorbents for Hg⁰ removal from coal derived fuel gas: effect of hydrogen chloride, *Fuel* 87 (2008) 467–474.
- [10] H. Yang, Z. Xu, M. Fan, A.E. Bland, R.R. Judkins, Adsorbents for capturing mercury in coal-fired boiler flue gas, *J. Hazard. Mater.* 146 (2007) 1–11.
- [11] E.J. Granite, M.C. Freeman, R.A. Hargis, W.J. O'Dowd, H.W. Pennline, The thief process for mercury removal from flue gas, *J. Environ. Manage.* 84 (2007) 628–634.
- [12] Z.-k. Zhuang, Z.-m. Yang, S.-y. Zhou, H.-q. Wang, C.-l. Sun, Z.-b. Wu, Synergistic photocatalytic oxidation and adsorption of elemental mercury by carbon modified titanium dioxide nanotubes under visible light LED irradiation, *Chem. Eng. J.* 253 (2014) 16–23.
- [13] J. Li, N. Yan, Z. Qu, S. Qiao, S. Yang, Y. Guo, P. Liu, J. Jia, Catalytic oxidation of elemental mercury over the modified catalyst Mn/α-Al₂O₃ at lower temperatures, *Environ. Sci. Technol.* 44 (2009) 426–431.
- [14] X. Chen, Titanium dioxide nanomaterials and their energy applications, *Chin. J. Catal.* 30 (2009) 839–851.
- [15] X. Chen, S.S. Mao, Titanium dioxide nanomaterials: synthesis, properties, modifications, and applications[J], *Chem. Rev.* 107 (7) (2007) 2891–2959.
- [16] R. Wang, X. Cai, F. Shen, TiO₂ hollow microspheres with mesoporous surface: superior adsorption performance for dye removal, *Appl. Surf. Sci.* 305 (2014) 352–358.
- [17] H. Zhang, Y. Song, Y. Sheng, H. Li, Z. Shi, X. Xu, H. Zou, EDTA-assisted fabrication of TiO₂ core-shell microspheres with improved photocatalytic performance, *Ceram. Int.* 41 (2015) 247–252.
- [18] N. Alenzi, W.-S. Liao, P.S. Cremer, V. Sanchez-Torres, T.K. Wood, C. Ehlig-Economides, Z. Cheng, Photoelectrochemical hydrogen production from water/methanol decomposition using Ag/TiO₂ nanocomposite thin films, *Int. J. Hydrogen Energy* 35 (2010) 11768–11775.

- [19] S.-S. Chen, H.-C. Hsi, S.-H. Nian, C.-H. Chiu, Synthesis of N-doped TiO₂ photocatalyst for low-concentration elemental mercury removal under various gas conditions, *Appl. Catal. B: Environ.* 160–161 (2014) 558–565.
- [20] H. Li, C.-Y. Wu, Y. Li, J. Zhang, Superior activity of MnO_x-CeO₂/TiO₂ catalyst for catalytic oxidation of elemental mercury at low flue gas temperatures, *Appl. Catal. B: Environ.* 111–112 (2012) 381–388.
- [21] J. Yang, Q. Yang, J. Sun, Q. Liu, D. Zhao, W. Gao, L. Liu, Effects of mercury oxidation on V₂O₅-WO₃/TiO₂ catalyst properties in NH₃-SCR process, *Catal. Commun.* 59 (2015) 78–82.
- [22] H. Li, C.-Y. Wu, Y. Li, L. Li, Y. Zhao, J. Zhang, Impact of SO₂ on elemental mercury oxidation over CeO₂-TiO₂ catalyst, *Chem. Eng. J.* 219 (2013) 319–326.
- [23] S. Xu, A.J. Du, J. Liu, J. Ng, D.D. Sun, Highly efficient CuO incorporated TiO₂ nanotube photocatalyst for hydrogen production from water, *Int. J. Hydrogen Energy* 36 (2011) 6560–6568.
- [24] J. Yu, Y. Hai, M. Jaroniec, Photocatalytic hydrogen production over CuO-modified titania, *J. Colloid Interface Sci.* 357 (2011) 223–228.
- [25] J. Bandara, C.P.K. Udawatta, C.S.K. Rajapakse, Highly stable CuO incorporated TiO₂ catalyst for photocatalytic hydrogen production from H₂O, *Photochem. Photobiol. Sci.* 4 (2005) 857–861.
- [26] D. Barreca, P. Fornasiero, A. Gasparotto, V. Gombac, C. Maccato, T. Montini, E. Tondello, The potential of supported Cu₂O and CuO nanosystems in photocatalytic H₂ production, *ChemSusChem* 2 (2009) 230–233.
- [27] L.S. Yoong, F.K. Chong, B.K. Dutta, Development of copper-doped TiO₂ photocatalyst for hydrogen production under visible light, *Energy* 34 (2009) 1652–1661.
- [28] X.Z. Ding, X.H. Liu, Y.Z. He, Grain size dependence of anatase-to-rutile structural transformation in gel-derived nanocrystalline titania powders, *J. Mater. Sci. Lett.* 15 (1996) 1789–1791.
- [29] S. Brunauer, P.H. Emmett, E. Teller, Adsorption of gases in multimolecular layers, *J. Am. Chem. Soc.* 60 (1938) 309–319.
- [30] E.P. Barrett, L.G. Joyner, P.P. Halenda, The determination of pore volume and area distributions in porous substances. I. Computations from nitrogen isotherms, *J. Am. Chem. Soc.* 73 (1951) 373–380.
- [31] V. Gombac, L. Sordelli, T. Montini, J.J. Delgado, A. Adamski, G. Adami, M. Cargnello, S. Bernal, P. Fornasiero, CuO_x-TiO₂ photocatalysts for H₂ production from ethanol and glycerol solutions, *J. Phys. Chem. A* 114 (2009) 3916–3925.
- [32] D. Chadda, J.D. Ford, M.A. Fahim, Chemical energy storage by the reaction cycle CuO/Cu₂O, *Int. J. Energy Res.* 13 (1989) 63–73.
- [33] E.J. Elzinga, R.J. Reeder, X-ray absorption spectroscopy study of Cu²⁺ and Zn²⁺ adsorption complexes at the calcite surface: implications for site-specific metal incorporation preferences during calcite crystal growth, *Geochim. Cosmochim. Acta* 66 (2002) 3943–3954.
- [34] Z. Wu, B. Jiang, Y. Liu, Effect of transition metals addition on the catalyst of manganese/titania for low-temperature selective catalytic reduction of nitric oxide with ammonia, *Appl. Catal. B: Environ.* 79 (2008) 347–355.
- [35] S. Hu, F. Zhou, L. Wang, J. Zhang, Preparation of Cu₂O/CeO₂ heterojunction photocatalyst for the degradation of acid orange 7 under visible light irradiation, *Catal. Commun.* 12 (2011) 794–797.
- [36] Z. Jin, X. Zhang, Y. Li, S. Li, G. Lu, 5.1% apparent quantum efficiency for stable hydrogen generation over eosin-sensitized CuO/TiO₂ photocatalyst under visible light irradiation, *Catal. Commun.* 8 (2007) 1267–1273.
- [37] W.-T. Chen, V. Jovic, D. Sun-Waterhouse, H. Idriss, G.I.N. Waterhouse, The role of CuO in promoting photocatalytic hydrogen production over TiO₂, *Int. J. Hydrogen Energy* 38 (2013) 15036–15048.
- [38] W. Xu, H. Wang, X. Zhou, T. Zhu, CuO/TiO₂ catalysts for gas-phase Hg⁰ catalytic oxidation, *Chem. Eng. J.* 243 (2014) 380–385.
- [39] B. Wang, Q. Li, W. Wang, Y. Li, J. Zhai, Preparation and characterization of Fe³⁺-doped TiO₂ on fly ash cenospheres for photocatalytic application, *Appl. Surf. Sci.* 257 (2011) 3473–3479.
- [40] Y. Yuan, J. Zhang, H. Li, Y. Li, Y. Zhao, C. Zheng, Simultaneous removal of SO₂, NO and mercury using TiO₂-aluminum silicate fiber by photocatalysis, *Chem. Eng. J.* 192 (2012) 21–28.
- [41] M. Anpo, Preparation, characterization, and reactivities of highly functional titanium oxide-based photocatalysts able to operate under UV–visible light irradiation: approaches in realizing high efficiency in the use of visible light, *Bull. Chem. Soc. Jpn.* 77 (2004) 1427–1442.
- [42] Y. Jiang, P. Zhang, Z. Liu, F. Xu, The preparation of porous nano-TiO₂ with high activity and the discussion of the cooperation photocatalysis mechanism, *Mater. Chem. Phys.* 99 (2006) 498–504.
- [43] Z.H. Wang, S.D. Jiang, Y.Q. Zhu, J.S. Zhou, J.H. Zhou, Z.S. Li, K.F. Cen, Investigation on elemental mercury oxidation mechanism by non-thermal plasma treatment, *Fuel Process. Technol.* 91 (2010) 1395–1400.
- [44] L. Jia, R. Dureau, V. Ko, E.J. Anthony, Oxidation of mercury under Ultraviolet (UV) irradiation, *Energy Fuels* 24 (2010) 4351–4356.
- [45] Y. Liu, J. Zhang, Z. Wang, A study on kinetics of NO absorption from flue gas by using UV/Fenton wet scrubbing, *Chem. Eng. J.* 197 (2012) 468–474.
- [46] G. Snider, P. Ariya, Photo-catalytic oxidation reaction of gaseous mercury over titanium dioxide nanoparticle surfaces, *Chem. Phys. Lett.* 491 (2010) 23–28.
- [47] S.G. Botta, D.J. Rodríguez, A.G. Leyva, M.I. Litter, Features of the transformation of Hg^{II} by heterogeneous photocatalysis over TiO₂, *Catal. Today* 76 (2002) 247–258.
- [48] M.S. Gustin, S.E. Lindberg, P.J. Weisberg, An update on the natural sources and sinks of atmospheric mercury, *Appl. Geochem.* 23 (2008) 482–493.
- [49] T. Montini, V. Gombac, L. Sordelli, J.J. Delgado, X. Chen, G. Adami, P. Fornasiero, Nanostructured Cu/TiO₂ photocatalysts for H₂ production from ethanol and glycerol aqueous solutions, *ChemCatChem* 3 (2011) 574–577.